analytical chemistry

pubs.acs.org/ac Article

"Dual-Signal-On" Integrated-Type Biosensor for Portable Detection of miRNA: Cas12a-Induced Photoelectrochemistry and Fluorescence Strategy

Haoran Shen, Aori Qileng, Hui Yang, Hongzhi Liang, Hongshuai Zhu, Yingju Liu,* Hongtao Lei,* and Weipeng Liu*

Cite This: *Anal. Chem.* 2021, 93, 11816−11825 Read Online

ACCESS | Metrics & More | Article Recommendations | Supporting Information

ABSTRACT: The abnormal expression of microRNA (miRNA) can affect the RNA transcription and protein translation, leading to tumor progression and metastasis. Currently, the accurate detection of aberrant expression of miRNA, particularly using a portable detection system, remains a great challenge. Herein, a novel dual-mode biosensor with high sensitivity and robustness for miR-21 detection was developed based on the cis-cleavage and trans-cleavage activities of Cas12a. miRNA can be combined with hairpin DNA-horseradish peroxidase anchored on a CdS/g-C_3N_4/B-TiO_2 photoelectrode, thus the nonenzymatic amplification was triggered to form numerous HRP-modified double-stranded DNA (HRP-dsDNA). Then, HRP-dsDNA can be specifically recognized and efficiently cis-cleaved by Cas12a nucleases to detach HRP from the substrate, while the remaining HRP on HRP-dsDNA can catalyze 4-chloro-1-naphthol (4-CN) to form biocatalytic precipitation (BCP) on the surface of the photoelectrode, and thus the photocurrent can be changed. Meanwhile, the trans-cleavage ability of Cas12a was activated, and nonspecifically degrade the FQ-reporter and a significant fluorescence signal can be generated. Such two different kinds of signals with independent transmission paths can mutually support to improve the performance of the detection platform. Besides, a portable device was constructed for the point-of-care (POC) detection of miR-21. Moreover, the dual-mode detection platform can be easily expanded for the specific detection of other types of biomarkers by changing the sequence of hairpin DNA, thereby promoting the establishment of POC detection for early cancer diagnosis.

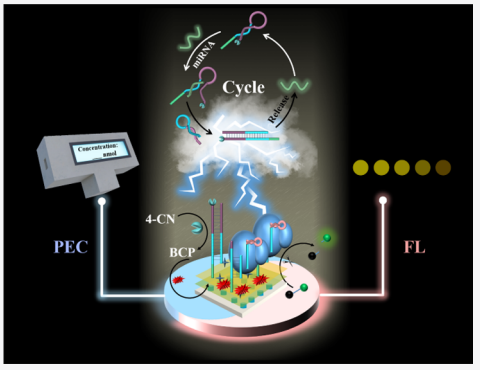

1. INTRODUCTION

miRNAs are endogenous and noncoding small single-strand RNAs (approximately 18−25 nt in length) that are widely found in animals, plants, and viruses.[1,2] Moreover, miRNAs play an essential role in gene regulation, such as cell development, differentiation, metabolism, and apoptosis.[3−5] Currently, more than 2600 kinds of miRNA in humans have been discovered to regulate various parts of the biotic process.[6] Besides, a single or a few miRNAs can control hundreds of mRNA, and thus form an intertwined regulatory network with genes and proteins.[7,8] Due to the powerful regulatory function of miRNAs, more attention has been paid to the relevance and function of miRNAs in human diseases. Significantly, more than half of human miRNA genes had been found in the fragile zones of chromosomes. The genes within these regions are generally mutated and have an abnormal expression when cancer occurs. It is suggested that tumorigenesis and tumor progression may affect the expression level of miRNAs,[1] thus miRNAs may act as a potential clinical biomarker for detecting early-stage cancers.[9−11] However, due to the low abundance, high homology, and easy degradation of miRNA, an accurate miRNA analysis is still a challenge.[12] Therefore, a sensitive, reliable, and portable biosensor for miRNA detection is urgently required.

Researchers have developed various methods for miRNA detection, including microarray, Northern blotting, and RT-PCR.[13−15] Although the above traditional methods have high sensitivity, complicated operation and expensive equipment limit their development. Recently, a series of detection platforms have been explored, such as nucleic acid amplification strategy combined with surface-enhanced Raman spectroscopy (SERS),[16] electrochemistry,[17−19] colorimetry,[20] and fluorescence,[21] which can significantly improve the analytical performance. Especially, the photoelectrochemical (PEC) detector adopts the mode of different types of energy and total separation of light (excitation signal) and

Received: June 7, 2021
Accepted: August 6, 2021
Published: August 17, 2021

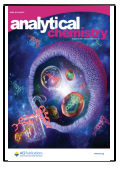

https://doi.org/10.1021/acs.analchem.1c02395
Anal. Chem. 2021, 93, 11816−11825

photocurrent (detection signal). Although PEC biosensor has various advantages including low background noise, low cost, and ultrahigh sensitivity and specificity,[22] the PEC detection platform was easily interfered with external environment factors.[23] To improve the accuracy and sensitivity of the detection platform, another individual response signal is clearly necessary.[24] Different signals have completely independent transmission pathways, which can partly correct the errors caused by personnel operation and external condition factors.[25] Therefore, this work intends to construct a dual-mode biosensor for miR-21 detection.

For PEC biosensors, the performance depends on the photoactivity of photoelectronic materials. In recent years, metal oxide semiconductors (MOS) have been widely concerned. Among them, TiO_2 has been confirmed as an ideal material to construct PEC biosensors for its excellent photoelectric conversion performance, low biotoxicity, and outstanding electron transmission performance.[26] However, the specific surface area of TiO_2 was relatively small, which limited the photoelectric activity of TiO_2. Therefore, by in situ etching of TiO_2, branch TiO_2 (B-TiO_2) was formed with numerous branches on the surface of TiO_2.[27] With a larger specific surface area of B-TiO_2, more active sites were exposed and the photoelectric conversion performance was improved.[28] Nevertheless, the band gap limitation of B-TiO_2 still limits its excitation only at ultraviolet radiation, which can inactivate the activity of biomolecules. The construction of semiconductor heterojunctions is an efficient method for inhibiting the recombination of holes and photogenerated electrons in semiconductor materials.[29] Therefore, the narrow-band semiconductor can be used as a sensitizer to modify B-TiO_2 to construct binary nanocomposites, which can significantly expand the absorption of visible light as well as promote electron transmission and enhance the photo-to-current stability. Since the conduction band (CB) of these narrow-band semiconductors is higher than that of the CB of B-TiO_2, it can promote the photogenerated electrons flow from the higher CB to the lower CB.[30] Herein, a ternary CdS/g-C_3N_4/B-TiO_2 photoactive material was synthesized by combining B-TiO_2 with two narrow band gap semiconductors. Due to their stepwise band levels, not only the visible-light absorption capacity but also the effective separation of the photogenerated holes and electrons can be improved, accordingly improving the stability and photoelectric conversion efficiency.

The clustered regularly interspaced short palindromic repeats (CRISPR) is a revolutionary gene-editing technology widely used in the genetic engineering of animals, plants, and bacteria.[31] Due to its excellent nucleic acid recognition performance and nonspecificity nucleic acid cleavage function (trans-cleavage) after activation, CRISPR/Cas12a, CRISPR/Cas13a, and CRISPR/Cas14a nucleases have caused widespread concern in the field of molecular diagnostics and biosensing. Cas12a is an RNA-guide dsDNA-targeting effector by the strict complementarity-dependent cis-cleavage principle, which shows very high exactness in the recognition of target nucleic acid. In addition, after recognizing the target, the trans-cleavage performance of Cas12a can be activated, which indiscriminately cleaves all single-strand DNA (ssDNA) nearby.[32] Therefore, the CRISPR/Cas12a system can enhance the sensitivity and specificity of the detection. Recently, a series of detection platforms combined with CRISPR/Cas12a, such as DNA endonuclease targeted CRISPR trans reporter (DETECTR)[33] and aTF-mediated small-molecule detector (CaT-Smelor),[34] and one-hour low-cost multipurpose highly efficient system (HOLMES)[35] have been developed. To further promote the application of Cas12a in the field of practical analysis, Cas12a was combined with aptamer[36] and DNA logic circuits to achieve sensitive detection of different substances.[37,38] In this study, CRISPR/Cas12a was applied in PEC and fluorescence detection, which can achieve the improvement of sensitivity and specificity of the dual-mode detection strategy.

Herein, a CRISPR/Cas12a-associated dual-mode miRNA detection platform was constructed based on PEC and fluorescence response. The CdS/g-C_3N_4/B-TiO_2 photoelectrode with excellent photo-to-current conversion was used as the efficient photoelectric substrate to immobilize hairpin DNA-horseradish peroxidase. Then, miRNA could initiate nonenzymatic amplification to produce large amounts of HRP-dsDNA that can be explicitly recognized by Cas12a. Subsequently, Cas12a can cis-cleave dsDNA to make HRP detach from the surface of photoelectrode. The remaining HRP on the HRP-dsDNA can catalyze 4-chloro-1-naphthol (4-CN) to form biocatalytic precipitation (BCP) on the surface of photoelectrode and finally causes a significant change in the photocurrent. Meanwhile, the trans-cleavage function of Cas12a can be activated, which can efficiently cleave FQ-reporter (5′ FAM-$(A)_5$-BHQ1 3′) around it and engender a remarkable fluorescent signal. To enhance the portability of the sensing platform, we integrate the signal converter and three-electrode signal amplification system into the portable device, which may provide a new solution for sensitive and point-of-care (POC) detection for miRNA and promote the application of the CRISPR/Cas system.

2. EXPERIMENTAL SECTION

2.1. Preparation of Hairpin Probe and crRNA. All of the sequences of oligonucleotides are provided in Table S1 of the Supporting Information. The hairpin probes H1 and H2 were diluted to 1 μM in annealing buffer (20 mM Tris, 140 mM NaCl, 5 mM KCl, pH 7.4). After that, the solution was heated to 95 °C for 10 min, and then tardily cooled to 20 °C at the rate of 1.5 °C·min^{-1} to make the probe fold into the hairpin structure. Then, the HRP-conjugated streptavidin (0.4 mg·mL^{-1}) was added into the annealed solution of H1 (1 μM) at room temperature for 90 min to form HRP-modified H1 (HRP-H1). Finally, the prepared hairpin probes were stored at −20 °C until use.

As for the preparation of crRNA, the oligonucleotides containing the T7 promoter and template sequence (crRNA-TS) were annealed with a T7 complementary strand (crRNA-CS) to form the DNA template (final concentrations 500 nM), which was used in vitro transcription. The constituents included 2 μL of 500 nM annealed product, 2 μL of RNA polymerase reaction buffer, 100 U of T7 RNA polymerase, 20 U of Ribnuclease inhibitor, and 12.5 μL of DEPC-treated water; the total volume was 20 μL. The transcription reaction was maintained at 37 °C for 4 h. After that, the above solution was heated at 95 °C for 10 min and quickly cooled down to 4 °C to completely inactivate the T7 RNA polymerase. Subsequently, the resulting solution was added to the mixture of 6 U of deoxyribonuclease I (DNase I), 10 μL of DNase reaction buffer, and 67 μL of DEPC-treated water, which was incubated at 37 °C for 1.5 h to remove the DNA templates. Then, the solution was heated at 80 °C for 10 min to ensure

https://doi.org/10.1021/acs.analchem.1c02395
Anal. Chem. 2021, 93, 11816−11825

Scheme 1. Strategy of the Dual-Mode Biosensor for Detecting miRNA

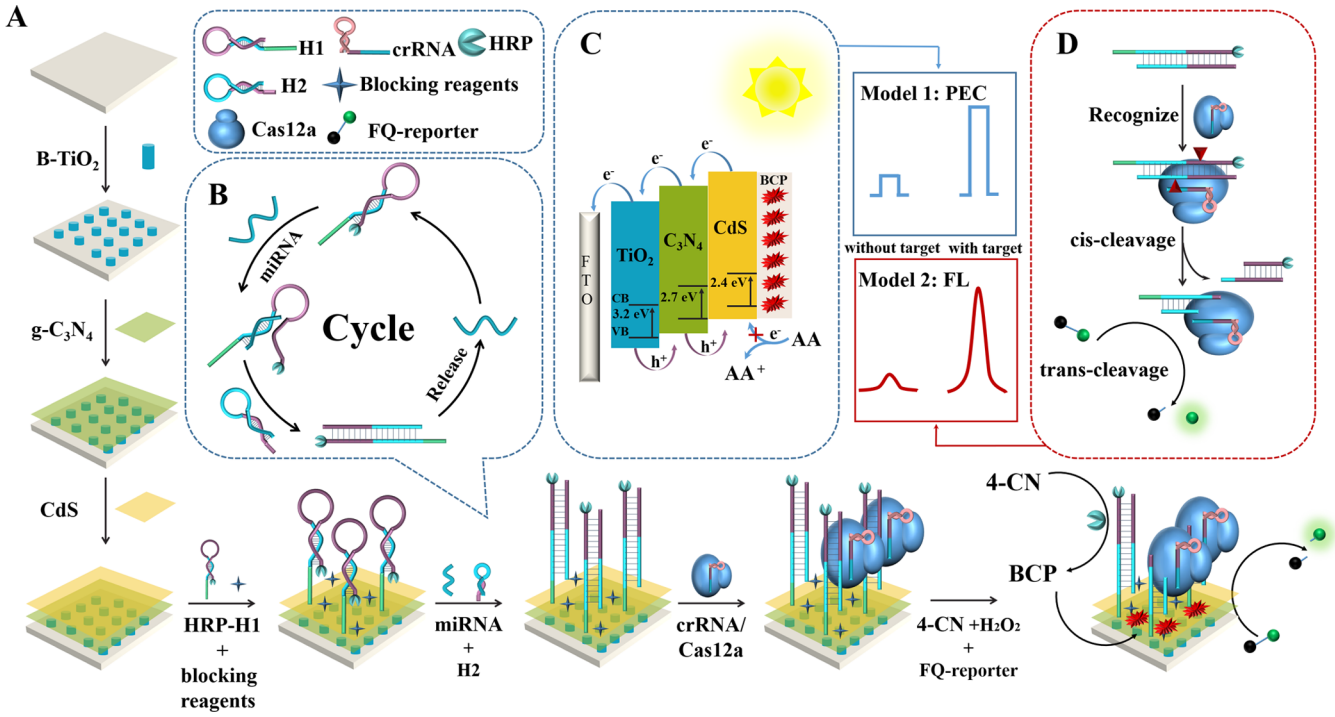

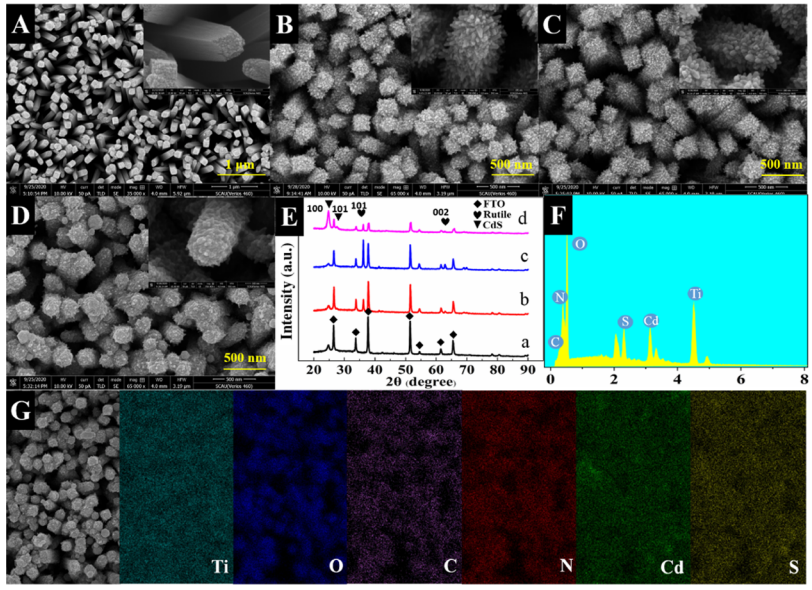

Figure 1. SEM images of (A) TiO_2, (B) B-TiO_2, (C) g-C_3N_4/B-TiO_2, and (D) CdS/g-C_3N_4/B-TiO_2 at different magnifications. (E) XRD spectrum of (a) FTO, (b) B-TiO_2, (c) g-C_3N_4/B-TiO_2, and (d) CdS/g-C_3N_4/B-TiO_2. (F) EDS analysis of CdS/g-C_3N_4/B-TiO_2. (G) Elemental mapping of CdS/g-C_3N_4/B-TiO_2.

that the DNase I was inactivated. The product was stored at −20 °C until subsequent use.

2.2. Fabrication of a Dual-Mode PEC and Fluorescence Biosensor for miR-21 Sensing. CdS/g-C_3N_4/B-TiO_2/FTO was prepared as the substrate of PEC detection (Supporting information). The constructive strategy of a dual-mode PEC and fluorescence biosensor was shown in Scheme 1. First, the CdS/g-C_3N_4/B-TiO_2/FTO photoelectrode was divided into small chips (25 mm × 5 mm). Then, the chip was immersed in an aqueous solution containing 87 mg·mL^{-1} L-cysteine hydrochloride for 2 h to introduce carboxyl groups on the surface of the photoelectrode. Subsequently, the as-prepared photoelectrode was washed with phosphate-buffered saline (PBS, pH 7.4) and carboxyl groups were activated by the EDC/NHS mixture (20/10 mg·mL^{-1}) for 60 min at 37 °C water bath. Afterward, 20 μL of HRP-H1 was dropped and incubated at 37 °C for 60 min. Then, the photoelectrode was rinsed with PBS, dried, and blocked with 20 μL of blocking reagents for 60 min. The dual-mode sensing platform of miR-21 was based on the performance of Cas12a. The mixture I containing 10 μL of H2 (1 μM) and 10 μL of miR-21 with different concentrations were dropped onto the surface of the

https://doi.org/10.1021/acs.analchem.1c02395
Anal. Chem. 2021, 93, 11816−11825

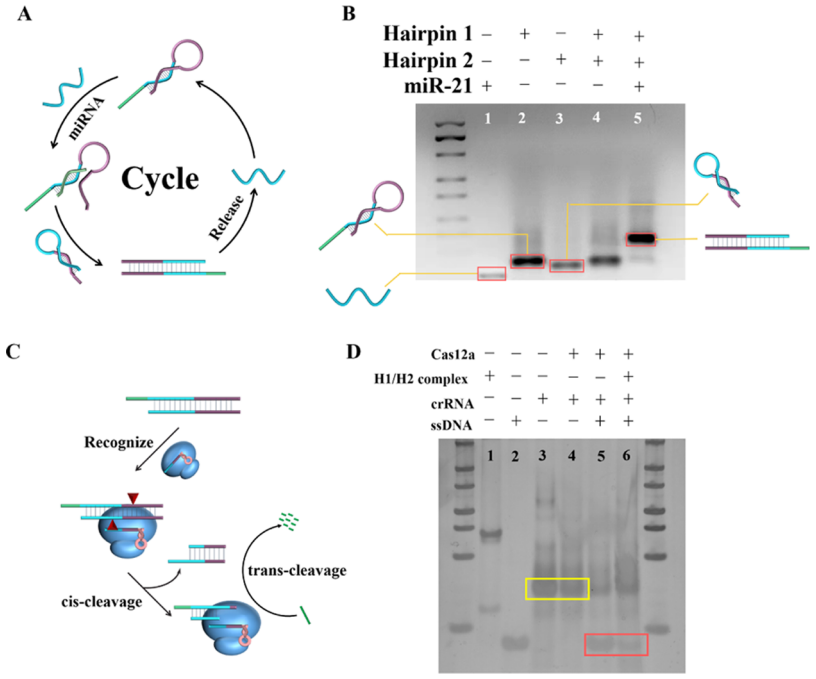

Figure 2. (A) Principle of nonenzymatic amplification. (B) Agarose gel electrophoresis of (lane 1) miR-21, (lane 2) H1, (lane 3) H2, (lane 4) H1 + H2, and (lane 5) miR-21 + H1 + H2 (nucleic acid stain: ethidium bromide). (C) Cleavage mechanism of Cas12a. (D) PAGE analysis of the cleavage of Cas12a. (lane 1) H1/H2 complex, (lane 2) ssDNA, (lane 3) crRNA, (lane 4) Cas12a and crRNA, (lane 5) crRNA, Cas12a, and ssDNA, and (lane 6) Cas12a, crRNA, ssDNA, and H1/H2 complex.

photoelectrode at 37 °C for 30 min. Then, 20 μL of crRNA/Cas12a complex (the amount of Cas12a was 1 pmol) was further incubated on the photoelectrode for 30 min at 37 °C. Finally, the photoelectrode was immersed in mixture II containing 1 mM 4-CN, 1 mM H_2O_2, and 10 μM FQ-reporter, washed with 10 mM phosphate-buffered saline with Tween-20 (PBST) and dried, then the corresponding photocurrent was measured in 0.1 M ascorbic acid (AA). Furthermore, the fluorescence of mixture II was measured at an excitation wavelength of 470 nm.

3. RESULTS AND DISCUSSION

3.1. Detection Strategy. Herein, a dual-mode biosensor based on Cas12a was proposed for the detection of miR-21. As shown in Scheme 1, HRP-H1 was assembled on the photoelectrode surface through an amide bond. Subsequently, as shown in Scheme 1B, the target miR-21 combined with HRP-H1 to form the miRNA/HRP-H1 complex. Thus, a single-stranded toehold of H1 was exposed, which can bind with H2. A branch migration reaction was triggered to form an HRP-H1/H2 duplex (HRP-dsDNA), thus miR-21 was displaced from HRP-H1. The released miR-21 can bind with another HRP-H1 to initiate the cyclical DNA strand displacing reaction, producing amounts of HRP-dsDNA that can be specifically recognized by Cas12a (Scheme 1B). As shown in Scheme 1D, the accumulated HRP-dsDNA was cleaved by Cas12a/crRNA complex. First, the cis-cleavage can detach HRP from the surface of the photoelectrode, while the remaining HRP on HRP-dsDNA can catalyze 4-CN to form BCP on the surface of photoelectrode (Scheme 1C). The insoluble precipitation can inhibit the electron transfer between the solid and liquid limiting surface, hinder the optical absorption of CdS/g-C_3N_4/B-TiO_2/FTO and restrict the diffusion of sacrificial reagent. As a result, the current of the photoelectrode was changed. Second, the trans-cleavage activity was simultaneously initiated, in which the FQ-reporter was cleaved and the previously quenched fluorescence was turned on. Thus, the change of photocurrent and fluorescence intensity allows the dual-mode sensor to detect miR-21 with high sensitivity and specificity.

3.2. Characterization of CdS/g-C_3N_4/B-TiO_2/FTO. The surface morphology of CdS/g-C_3N_4/B-TiO_2 was characterized by SEM. Figure 1A shows the top view of TiO_2 at different magnifications. It can be seen that TiO_2 was grown perpendicularly on the FTO with a radius of the apex of about 55 nm. Figure 1B is the top view of B-TiO_2 at different scales, in which a large number of small branches are grown on the wall of TiO_2. The B-TiO_2 with a large density of branches was favorable to the absorption of light. Figure 1C is the top view of g-C_3N_4/B-TiO_2 in different scales, where the width of branches increases a little. After the CdS nanoparticles were deposited on g-C_3N_4/B-TiO_2 by chemical deposition, the morphology was considerably changed, where the branches were coated with a layer of precipitates (Figure 1D). Figure 1E (curve d) was the XRD pattern of CdS/g-C_3N_4/B-TiO_2, where the peaks of 36.5° and 64.3° corresponded to the (101) and (002) of the TiO_2 crystal (JCPDS no. 21-1276), and the different peaks at 26.7° and 28.1° showed the characteristic (100) and (101) reflections of CdS (JCPDS no. 74-0534). Due to the low content of g-C_3N_4, the characteristic peaks of g-C_3N_4 were not obvious. EDS of CdS/g-C_3N_4/B-TiO_2 was further performed and the results are given in Figure 1F, where elements including Ti, O, C, N, Cd, and S can be found. Moreover, the weight percentage of C and N were 4.7 and 2.5%, respectively, indicating that the content of g-C_3N_4 was low. Figure 1G displays the element mapping of CdS/g-C_3N_4/B-TiO_2/FTO, which confirmed that C, N, S, and Cd are evenly dispersed on B-TiO_2.

https://doi.org/10.1021/acs.analchem.1c02395
Anal. Chem. 2021, 93, 11816−11825

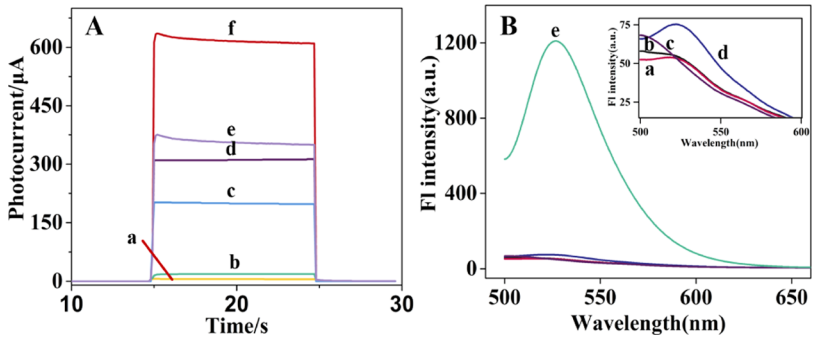

Figure 3. (A) Photoelectrochemical responses of (a) bare B-TiO_2, (b) g-C_3N_4/B-TiO_2, (c) detection system without miR-21, (d) CdS/B-TiO_2, (e) detection system with miR-21, and (f) CdS/g-C_3N_4/B-TiO_2. (B) Fluorescence responses of (a) 1 pM miR-21, (b) 100 μM H1, (c) 100 μM H2, (d) 100 μM H1 + 100 μM H2, and (e) 1 pM miR-21 + 100 μM H1 + 100 μM H2 in the solution of Cas12a/crRNA and FQ-reporter.

Figure S1 shows the UV−vis reflection spectra of B-TiO_2 (curve a), g-C_3N_4/B-TiO_2 (curve b), and CdS/g-C_3N_4/B-TiO_2 (curve c). The pure B-TiO_2 had intense absorption in the ultraviolet region at about 400 nm and a band gap of 3.2 eV. When g-C_3N_4 was in situ deposited onto the B-TiO_2 substrate, g-C_3N_4/B-TiO_2 showed an optical absorption edge with no significant change. Nevertheless, the absorption intensity of visible light had a certain increase, which indicated that g-C_3N_4 can improve the photoelectric performance.[39] After the deposition of CdS onto the electrode, the absorption edge of CdS/g-C_3N_4/B-TiO_2 reached about 560 nm with a band gap of 2.4 eV. It is suggested that g-C_3N_4 can improve the light absorption ability of the material, and CdS can significantly improve the absorption of the material in the visible-light region.[40] Therefore, XPS was used to further study the chemical bonding and valence elements of CdS/g-C_3N_4/B-TiO_2 composites. The full-scan XPS spectrum (Figure S2A) shows that Ti, O, C, N, Cd, and S had the corresponding remarkable peaks and each element (Figure S2B−G) was analyzed as follows. Ti 2p had two remarkable absorption peaks at 464.1 eV (Ti $2p_{1/2}$) and 458.3 eV (Ti $2p_{3/2}$), and the interval between two peaks of Ti 2p was 5.7 eV, indicating the normal state of Ti^{4+} and the corresponding Ti−O.[41] Besides, two peaks of 463.3 and 458.5 eV were assigned to $2p_{1/2}$ and $2p_{3/2}$, respectively, indicating that self-doped Ti^{3+} was formed in TiO_2. Ti^{3+} can inhibit the recombination of electron−hole pairs and promote charge separation.[42] Two O peaks also appeared at 531.4 and 529.6 eV, corresponding to the Ti−O group and the hydroxyl group on the surface of the material, respectively. In the spectrum of C 1s, four peaks at 288.6, 285.8, 284.9, and 284.3 eV were assigned to C−S, N−C═N, C−$(N)_3$, and C−C, respectively.[43] In the N 1s spectrum, the peaks at 405.4, 404.9, and 404.5 eV were derived from NH_2, N−$(C)_3$, and N═C, respectively.[44] The spectrum of C 1s and N 1s implied that the carbon atom was bond with a nitrogen atom to form g-C_3N_4. In the spectrum of Cd 3d, two remarkable peaks at 411.7 eV (Cd $3d_{3/2}$) and 409.9 eV (Cd $3d_{5/2}$) were found. Two peaks also appeared at 162.4 eV (S $2p_{1/2}$) and 161.3 eV (S $2p_{3/2}$).[45] Therefore, CdS/g-C_3N_4/B-TiO_2 was successfully synthesized as a high-performance PEC material.

3.3. Feasibility of Nonenzymatic Amplification and the Cas12a-Mediated Cleavage. To verify the feasibility of a nonenzymatic amplification triggered by miR-21 (Figure 2A), electrophoresis analysis was performed using 3.5% agarose gel in the TBE buffer (Figure 2B). After the addition of miR-21, compared with H1 (lane 2) and H2 (lane 3) bands, a new H1/H2 complex band appeared (lane 5), indicating that miR-21 can initiate nonenzymatic amplification and the double-stranded structure was formed. On the contrary, when miR-21 was absent (lane 4), no band of the H1/H2 duplex was observed, indicating that the H1/H2 complex cannot be formed without the target miR-21.

To acquire high-quality crRNA, crRNA was translated and purified. The template strand for crRNA translation was obtained by annealing (Figure S3A). As shown in Figure S3B, compared with the template strand in lane 4, a bright band was seen in lane 1, indicating that crRNA was successfully synthesized. However, both crRNA-CS (lane 2) and crRNA-TS (lane 3) did not trigger the catalysis of T7 RNA polymerase, respectively. We used 12% polyacrylamide gel electrophoresis (PAGE) to analyze the performance of Cas12a. Then, by selecting a single-stranded DNA (ssDNA) as the trans-cleavage target, we obtained the cleavage reaction product of Cas12a shown in Figure 2D. Lanes 1, 2, and 3 were for H1/H2 complex, ssDNA, and crRNA, respectively. In lane 4, Cas12a and crRNA were added, and the band of crRNA significantly weakened (yellow marker), indicating that Cas12a and crRNA formed a binary complex. Lane 5 contained Cas12a, crRNA, and ssDNA, and the band of ssDNA did not disappear, indicating that the trans-cleavage performance of Cas12a cannot be activated without the H1/H2 complex. Lane 6 contained crRNA, Cas12a, ssDNA, and H1/H2 duplex. The intensity of the ssDNA band became weaker (red marker), indicating that the H1/H2 complex can activate the trans-cleavage performance of Cas12a to efficiently cleave ssDNA.

3.4. Detection Feasibility Assay. The detection feasibility of the dual-mode biosensor was confirmed through the photocurrent and fluorescent response. In the photoelectrochemical process, Figure 3A shows that B-TiO_2/FTO (curve a) and g-C_3N_4/B-TiO_2/FTO (curve b) offered a weak photocurrent response under visible-light irradiation. However, when CdS was deposited on g-C_3N_4/B-TiO_2/FTO (curve f), the photocurrent was significantly increased, about 30 times higher than that of g-C_3N_4/B-TiO_2/FTO. Meanwhile, compared with CdS/B-TiO_2/FTO (curve d), the photocurrent response was also significantly improved, which may be due to the fact that the ternary heterojunction structure can enhance the photocurrent.[46]

HRP can oxidize 4-CN to BCP (Figure S4), where a new characteristic peak at 520 nm appeared, attributed to the conjugation vibration of the benzene ring of BCP. Curves c and e (Figure 3A) show the photocurrent response when the concentrations of miR-21 are 0 and 1 pM, respectively. If the

https://doi.org/10.1021/acs.analchem.1c02395
Anal. Chem. 2021, 93, 11816−11825

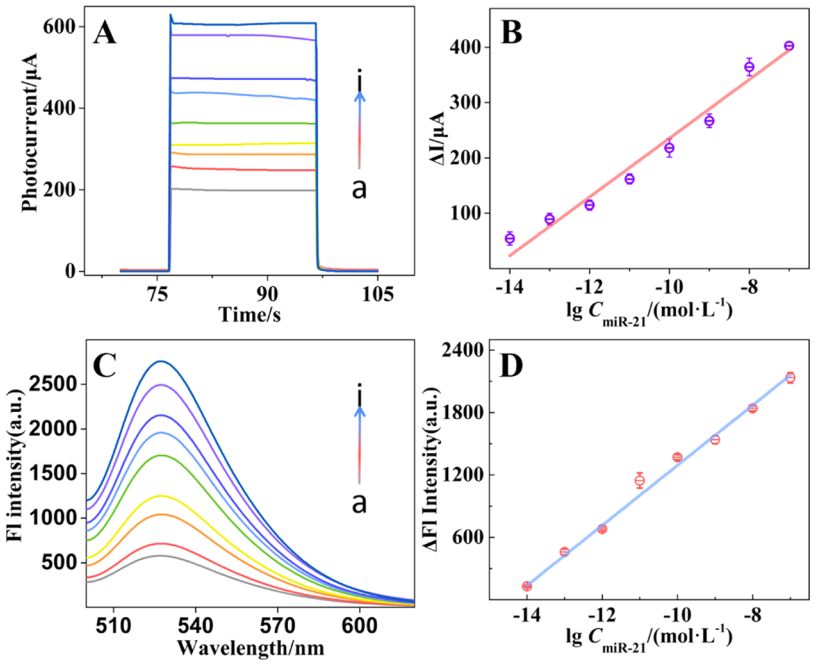

Figure 4. (A) Photocurrent response and (C) fluorescence response for different concentrations of miR-21, (a) blank, (b) 10 fM, (c) 100 fM, (d) 1 pM, (e) 10 pM, (f) 100 pM, (g) 1 nM, (h) 10 nM, and (i) 100 nM. Calibration curves of photocurrent response (B) and fluorescence response (D).

miR-21 was absent, the photocurrent was 205 μA (curve c). However, if the miR-21 concentration was 1 pM, the photocurrent was 332 μA (curve e). With the aid of miR-21, HRP-dsDNA can be formed on the surface of the photoelectrode and then cis-cleaved by Cas12a. Thus, the remaining HRP on HRP-dsDNA decreased, causing a decrease in the amount of BCP and the corresponding increase in the photocurrent. Therefore, the PEC method was suitable for the detection of miR-21 based on Cas12a.

In the fluorescence process, in Figure 3B, curve a shows that miR-21 cannot be recognized by Cas12a to initiate trans-cleavage performance. When the miR-21 was 0 absent, the fluorescence showed almost no response, which suggested that the mixture of H1 and H2 (curve d) did not activate the trans-cleavage activity of Cas12a. However, as shown in curve e, such a higher fluorescence intensity was discovered when the miR-21 concentration was 1 pM, since miR-21 could initiate nonenzymatic amplification to form a massive H1/H2 complex which can be recognized by Cas12a and activate trans-cleavage. Curves b and c showed that single H1 or single H2 cannot initiate the cleavage activity of Cas12a, respectively.

3.5. Optimization of the Detection Conditions. To achieve the optimal efficiency and sensitivity, several conditions were optimized, including the ratio of H1 and HRP, incubation time, amount of Cas12a, BCP time, pH, and concentration of AA. The ratio of H1 and HRP and incubation time were directly affected by the loading amount of HRP on the surface of the photoelectrode. As shown in Figure S5A, it can be found that the photocurrent significantly decreased with the increase in the ratio of H1 and HRP. However, when the ratio of H1 and HRP further increased, the photocurrent demonstrated no noticeable change. Therefore, the optimum ratio of H1 and HRP was 4:1. Meanwhile, the effect of the incubation time was also investigated (Figure S5B), since it can significantly influence the combination of H1-HRP with the photoelectrode. The photocurrent response rapidly decreased when the incubation time increased, while the photocurrent response was basically constant after 60 min. As a result, the optimum incubation time was 60 min. The amount of Cas12a was vital to ensure the cleavage of HRP-dsDNA (Figure S5C). For an enzymatic reaction mediated by Cas12a, if the amount of Cas12a was too low, the cleavage of the HRP-dsDNA was less and thus a weak change in photocurrent was discovered. Therefore, the optimum amount of Cas12a was 1 pmol. It is worth noting that the pH of the solution was also investigated since the acidity or alkalinity can have an impact on the activity of enzymes and the photocurrent response. As depicted in Figure S5D, in an acidic condition medium with a pH value from 5.0 to 6.8, the photocurrent decreased rapidly and reached a minimum at 6.8, while the photocurrent rapidly increased in the alkaline range, indicating that overly acidic and alkali can significantly influence the activity of enzymes. Therefore, a pH value of 6.8 was selected. The concentration of AA was thoroughly investigated in Figure S5E. When the AA concentration was lower than 0.1 M, the photocurrent increased with the increase in the concentration of AA, since the photogenerated holes were gradually filled by electrons provided by AA. When the AA concentration was more than 0.15 M, the photocurrent showed a slight decrease, since excess AA can influence the acid−base balance of the biosensor or slightly destruct the biological structure. Thus, 0.1 M AA was selected. As in Figure S5F, by optimizing the BCP time, it is seen that the PEC response decreased notably with the extension of the BCP time and reached a stable value when the BCP time was 20 min, so 20 min was selected.

3.6. Analytical Performance of the Dual-Mode Detection Platform. Under the optimal conditions, using CdS/g-C_3N_4/B-TiO_2/FTO as the photoelectrode and Cas12a as the recognition element, a dual-mode biosensor with PEC and fluorescence was constructed to detect miR-21. For the PEC detection, the biosensor without miR-21 cannot initiate nonenzymatic amplification and also cannot produce amounts

https://doi.org/10.1021/acs.analchem.1c02395
Anal. Chem. 2021, 93, 11816−11825

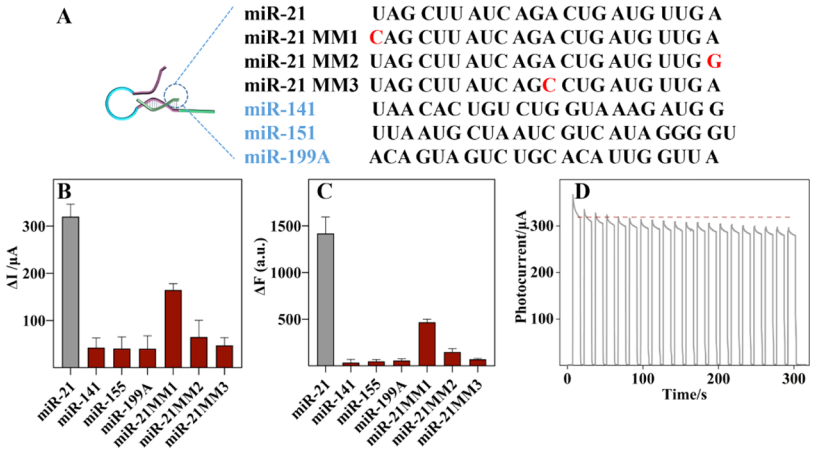

Figure 5. Specificity and stability of the dual-modal biosensor. (A) Sequences of different types of miRNAs. Photocurrent response (B) and fluorescence response (C) of the biosensor for different types of miRNAs. (D) Photocurrent stability of the proposed biosensor under 300 s continuous scanning.

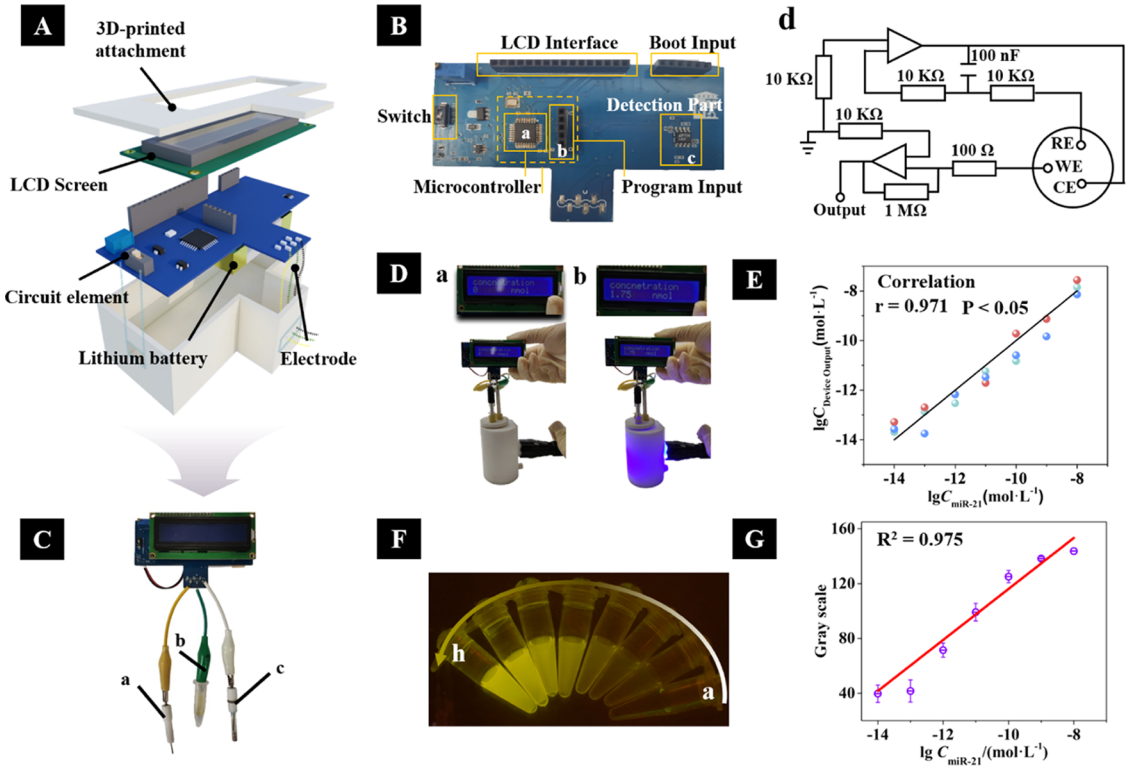

Figure 6. (A) Model diagram of the portable device. (B) Photo of the circuit element (a) microcontroller, (b) program input, (c) detection part, and (d) circuit diagram of detection part. (C) Image of the portable device. The performance of the portable device (D) when a 470 nm blue light was (a) turned off and (b) turned on. (E) Correlation analysis of PEC response. (F) Images for visual detection of miR-21 using the portable device, (a) blank, (b) 10 fM, (c) 100 fM, (d) 1 pM, (e) 10 pM, (f) 100 pM, (g) 1 nM, and (h) 10 nM. (G) Relationship between gray values and the logarithm of miR-21 concentrations.

of HRP-dsDNA to be specifically recognized by Cas12a. Therefore, a large amount of HRP can catalyze 4-CN to BCP, which could influence the light irradiation onto the photoelectrode and hinder electron transfer between the photoelectrode and AA solution, causing the photocurrent to drop to the minimum value (I_{min}). As shown in Figure 4A, the photocurrent increased with the concentration of miR-21 in the range of 10 fM to 100 nM. The photocurrent change (ΔI) can be obtained by subtracting the photocurrent at different concentrations of miR-21 from I_{min}. In Figure 4B, ΔI and the logarithm of the miR-21 concentration showed a good linear relationship, while the calibration equation was $\Delta I = 766.1 + 53.1[\lg C_{miR\text{-}21}\ (mol/L)]$ ($R^2 = 0.991$), and the limit of detection (LOD) was 5.8 fM (S/N = 3).

Meanwhile, the fluorescence intensity of the reaction solution was recorded for the supplementary fluorescent detection. In Figure 4C, when the concentration of miR-21 ranged from 10 fM to 100 nM, the fluorescence intensity significantly changed from 129 (a.u.) to 2134 (a.u.). As shown in Figure 4D, the calibration plot also displayed an excellent linear relationship between fluorescence response and the logarithm of miR-21 concentrations. The linear regression

https://doi.org/10.1021/acs.analchem.1c02395
Anal. Chem. 2021, 93, 11816−11825

equation was $\Delta F = 4181.2 + 289.0[\lg C_{miR\text{-}21}\ (mol/L)]$ with a LOD of 3.5 fM ($R^2 = 0.996$, S/N = 3). The dual-mode detection platform could produce two signals simultaneously, which were generated by independent transmission mechanisms. Such two signals could be compensated with each other to eliminate man-made errors or external factors. In addition, the combination of nonenzymatic amplification and dual-signal sensing effectively improved the accuracy and linear range of detection.

Due to the high homological similarity between different miRNAs, specificity is an essential indicator of the sensing platform. To evaluate the specificity of the dual-mode sensing platform, the sequences such as miR-141, miR-151, miR-199A, and single mismatched nucleotides of miR-21 (miR-21 MM1, miR-21 MM2, and miR-21 MM3) were chosen as possible distractors (Figure 5A). As in Figure 5B,C, the photocurrent response and fluorescence intensity for miR-21 were significantly higher than those for other miRNAs. Meanwhile, signal responses from miR-141, miR-151, and miR-199A were not significant compared with the blank control. Therefore, the detection platform had excellent specificity to detect miR-21. In the assay of miR-21 with a single mismatch nucleotide, the signal was slightly higher than that in the blank control. It was worth noting that miR-21 with a single-base mutation at the proximal end (miR-21 MM1) had a nonspecific signal response. These results indicated the single-base mismatch at the proximal end of miR-21 might initiate nonenzymatic amplification. In addition, miR-21 with a single-base mutation in the distal (miR-21 MM2) or middle (miR-21 MM3) cannot initiate nonenzymatic amplification, resulting not nonspecific signal response. Thus, the dual-mode detection platform had good specificity. Besides, it can distinguish miRNA, even single nucleotide mismatch. As in Figure 5D, when the concentration of miR-21 was 1 pM, the time-dependent photocurrent response was stable, indicating the stability was acceptable.

3.7. Portability of the Dual-Mode Detection Platform.

To enhance the practicability of the detection platform, the dual-mode detection strategy was combined with electronic components to develop a point-of-care (POC) device (Supporting Information). As shown in Figure 6A, the portable device is assembled from three sections including a LCD screen, detection circuit, and lithium battery. The detection circuit is composed of two main parts including the control chip part and the detection part. Figure 6Ba is the microcontroller Atmega328P-AU, which not only had program input and output ports (Figure 6Bb) but also had the function of an online upgrade program. Therefore, the program in the device can be updated to adapt to different detection environments and targets. The detection section was mainly composed of two parts. As in Figure 6Bc, the amplifier circuit chip of LT1426 can amplify the photocurrent from the three-electrode system, while the circuit diagram of the detection section is shown in Figure 6Bd. Besides, 5 V voltage was used as a power supply and a LCD screen was used to output the detection values. The three-electrode system was used to detect the photocurrent response using Pt as the counter electrode (Figure 6Ca), CdS/g-C_3N_4/B-TiO_2/FTO as the photoelectrode (Figure 6Cb), and Ag/AgCl as the reference electrode (Figure 6Cc). A 470 nm lamp was used for excitation and irradiation in the dual-mode portable detection platform.

Then, the PEC-fluorescence dual-mode miR-21 detection method was integrated into a small device. In the process of miR-21 detection, when the blue light was turned off, the value on the LCD was 0 nmol (Figure 6Da). Under blue light illumination, the miR-21 concentration appeared on the LCD (Figure 6Db), indicating that under a 470 nm blue light irradiation, the circuit can collect photocurrent change and convert it into the concentration of miR-21 through a built-in program. Therefore, to determine the availability of the device, correlation analysis was used to analyze the correlation between the output value of the device and the real concentration of miR-21. Figure 6E displays the regression line with a slope of approximately 1. The Pearson correlation coefficient reached the value of 0.972, indicating that the real concentration of miR-21 and output signal of the device correlate positively. Hence, this device can be used for miR-21 detection.

To verify the availability of fluorescence detection in the device, this portable device was used to detect different concentrations of miR-21. In Figure 6F, the fluorescence detection was performed under a 470 nm blue lamp. Under the blue light, the fluorescence intensity of the reaction system increased as the concentration of miR-21 increased. The photographs of fluorescence under different concentrations were taken, in which the gray scale values were recorded, and the values were linearly fitted with the logarithm of miR-21 concentrations. As in Figure 6G, in the concentration range from 10 fM to 10 nM, the gray value has a good linear relationship with the logarithm of miR-21 as the gray scale = $18.6 + 302.2[\lg C_{miR\text{-}21}\ (mol/L)]$ ($R^2 = 0.975$, S/N = 3). It is suggested that the device can realize the output of the fluorescence signal.

4. CONCLUSIONS

In summary, a novel dual-modal biosensor for ultrasensitive detection of miR-21 was constructed. Using the CdS/g-C_3N_4/B-TiO_2 ternary nanocomposite as the photoelectrode, hairpin nucleic acid mediated nonenzymatic amplification as signal amplification and Cas12a as the biomolecule recognition element. The integration of PEC sensing and fluorescence detection together could quickly detect miR-21 in the sample with high sensitivity and specificity. Under the optimal conditions, this dual-mode detection platform offered a linear PEC and fluorescence response with the miR-21 concentration in the range from 10 fM to 100 nM, with the low LODs of 5.8 fM (S/N = 3, PEC response) and 3.5 fM (S/N = 3, fluorescence response), respectively. Besides, a dual-mode detection strategy could be further integrated into a portable device, which can simplify the process of detection. In the future, high-throughput data collection and AI systems could be combined with the platform to finally achieve early cancer diagnosis on a portable biosensor platform.

■ ASSOCIATED CONTENT

Supporting Information

The Supporting Information is available free of charge at https://pubs.acs.org/doi/10.1021/acs.analchem.1c02395.

Materials, instruments, gel electrophoresis analysis, synthesis of CdS/g-C_3N_4/B-TiO_2/FTO, construction of a portable device, and the sequences of nucleic acid. UV−vis spectra of B-TiO_2, g-C_3N_4/B-TiO_2, and CdS/g-C_3N_4/B-TiO_2, full-scan XPS spectrum of the CdS/g-C_3N_4/B-TiO_2, and the deconvolution of Ti 2p, O 1s, C 1s, N 1s, Cd 3d, and S 2p, the agarose gel electrophoresis for the synthesis of DNA template and

https://doi.org/10.1021/acs.analchem.1c02395
Anal. Chem. 2021, 93, 11816−11825

synthesis of crRNA, effect of the ratio of H1 and HRP, the incubation time, the amount of Cas12a, the pH of the detection system, and the concentration of AA and the BCP time on the signal response of the biosensor (PDF)

AUTHOR INFORMATION

Corresponding Authors

Yingju Liu − *Key Laboratory for Biobased Materials and Energy of Ministry of Education, College of Materials and Energy, South China Agricultural University, Guangzhou 510642, China; Guangdong Provincial Key Laboratory of Food Quality and Safety, College of Food Science, South China Agricultural University, Guangzhou 510642, China;* orcid.org/0000-0002-1130-4945; Email: liuyingju@hotmail.com

Hongtao Lei − *Guangdong Provincial Key Laboratory of Food Quality and Safety, College of Food Science, South China Agricultural University, Guangzhou 510642, China;* orcid.org/0000-0002-1697-1747; Email: hongtao@scau.edu.cn

Weipeng Liu − *Key Laboratory for Biobased Materials and Energy of Ministry of Education, College of Materials and Energy, South China Agricultural University, Guangzhou 510642, China;* orcid.org/0000-0002-2153-1682; Email: weipeng_liu@scau.edu.cn

Authors

Haoran Shen − *Key Laboratory for Biobased Materials and Energy of Ministry of Education, College of Materials and Energy, South China Agricultural University, Guangzhou 510642, China*

Aori Qileng − *Key Laboratory for Biobased Materials and Energy of Ministry of Education, College of Materials and Energy, South China Agricultural University, Guangzhou 510642, China; Guangdong Provincial Key Laboratory of Food Quality and Safety, College of Food Science, South China Agricultural University, Guangzhou 510642, China*

Hui Yang − *Key Laboratory for Biobased Materials and Energy of Ministry of Education, College of Materials and Energy, South China Agricultural University, Guangzhou 510642, China*

Hongzhi Liang − *Key Laboratory for Biobased Materials and Energy of Ministry of Education, College of Materials and Energy, South China Agricultural University, Guangzhou 510642, China*

Hongshuai Zhu − *Key Laboratory for Biobased Materials and Energy of Ministry of Education, College of Materials and Energy, South China Agricultural University, Guangzhou 510642, China; Guangdong Provincial Key Laboratory of Food Quality and Safety, College of Food Science, South China Agricultural University, Guangzhou 510642, China*

Complete contact information is available at: https://pubs.acs.org/10.1021/acs.analchem.1c02395

Author Contributions

The manuscript was written through contributions of all authors.

Notes

The authors declare no competing financial interest.

ACKNOWLEDGMENTS

This work was supported by the National Natural Science Foundation of China (21874048 and 21705051), the Science and Technology Program of Guangzhou (202102020511), the National Key Research and Development Program of China (SQ2017YFC160089), the Educational Commission Foundation of Guangdong Province (2020ZDZX2025), and the Natural Science Foundation of Guangdong Province (2021A1515010208).

REFERENCES

(1) Lewis, B. P.; Burge, C. B.; Bartel, D. P. *Cell* **2005**, *120*, 15−20.
(2) Harrandah, A. M.; Mora, R. A.; Chan, E. K. L. *Cancer Lett.* **2018**, *438*, 126−132.
(3) Carthew, R. W.; Sontheimer, E. J. *Cell* **2009**, *136*, 642−655.
(4) Croce, C. M. *Nat. Rev. Genet.* **2009**, *10*, 704−714.
(5) Winter, J.; Jung, S.; Keller, S.; Gregory, R.; Diederichs, S. *Nat. Cell Biol.* **2009**, *11*, 228−234.
(6) Kozomara, A.; Griffiths, J. S. *Nucleic Acid Res.* **2014**, *42*, D68−D73.
(7) Pritchard, C. C.; Cheng, H. H.; Tewari, M. *Nat. Rev. Genet.* **2012**, *13*, 358−369.
(8) Treiber, T.; Treiber, N.; Meister, G. *Nat. Rev. Mol. Cell Biol.* **2019**, *20*, 5−20.
(9) Cimmino, A.; Calin, G. A.; Fabbri, M.; Iorio, M. V.; Ferracin, M.; Shimizu, M.; Wojcik, S. E.; Aqeilan, R. I.; Zupo, S.; Dono, M. G.; Rassenti, L. *Proc. Natl. Acad. Sci. USA* **2005**, *102*, 13944−13949.
(10) Hayes, J.; Peruzzi, P. P.; Lawler, S. *Trends Mol. Med.* **2014**, *20*, 460−469.
(11) Chen, X.; Xie, D.; Zhao, Q.; You, Z. H. *Briefings Bioinf.* **2019**, *20*, 515−539.
(12) Dong, H. F.; Lei, J. P.; Ding, L.; Wen, Y. Q.; Ju, H. X.; Zhang, X. J. *Chem. Rev.* **2013**, *113*, 6207−6233.
(13) Baker, M. *Nat. Methods* **2010**, *7*, 687−692.
(14) Streit, S.; Michalski, C. W.; Erkan, M.; Kleeff, J.; Friess, H. *Nat. Protoc.* **2009**, *4*, 37−43.
(15) Thomou, T.; Mori, M. A.; Dreyfuss, J. M.; Konishi, M.; Saaguchi, M.; Wolfrum, C.; Rao, T. N.; Winnay, J. N.; Garcia-Martin, R.; Grinspoon, S. K.; Gorden, P.; Kahn, R. *Nature* **2017**, *542*, 450−455.
(16) Pang, Y. F.; Wang, C. G.; Lu, L. C.; Wang, C. W.; Sun, Z. W.; Xiao, R. *Biosens. Bioelectron.* **2019**, *130*, 204−213.
(17) Cheng, W. T.; Ma, J. H.; Cao, P.; Zhang, Y. C.; Xu, C. J.; Yi, Y. X.; Li, J. L. *Talanta* **2020**, *219*, No. 121242.
(18) Zhao, M. L.; Zeng, W. J.; Chai, Y. Q.; Yuan, R.; Zhou, Y. *Anal. Chem.* **2020**, *92*, 11044−11052.
(19) Deng, H. M.; Chai, Y. Q.; Yuan, R.; Yuan, Y. L. *Anal. Chem.* **2020**, *92*, 8364−8370.
(20) Xia, Y. K.; Chen, T. T.; Zhang, L.; Zhang, X. L.; Shi, W. H.; Chen, G. Y.; Chen, W. Q.; Lan, J. M.; Li, C. Y.; Sun, W. M.; Chen, J. H. *Biosens. Bioelectron.* **2021**, *173*, No. 112834.
(21) Yang, L.; Fang, J.; Li, J. J.; Ou, X. Y.; Zhang, L.; Wang, Y. F.; Weng, Z.; Xie, G. M. *Anal. Chim. Acta* **2021**, *1143*, 157−165.
(22) Wei, J.; Chang, W. D.; Aori, Q. L.; Liu, W. P.; Zhang, Y.; Rong, S. Y.; Lei, H. T.; Liu, Y. J. *Anal. Chem.* **2018**, *90*, 9606−9613.
(23) Aori, Q. L.; Liang, H. Z.; Huang, S. L.; Liu, W. P.; Xu, Z. L.; Liu, Y. J. *Sens. Actuators, B* **2020**, *314*, No. 128066.
(24) Song, C. Y.; Jiang, X. Y.; Yang, Y. J.; Zhang, J. J.; Larson, S.; Zhao, Y. P.; Wang, L. H. *ACS Appl. Mater. Interfaces* **2020**, *12*, 31242−31254.
(25) Wei, J.; Chen, H. M.; Chen, H. H.; Cui, Y. Y.; Aori, Q. L.; Qin, W. W.; Liu, W. P.; Liu, Y. J. *ACS Appl. Mater. Interfaces* **2019**, *11*, 23832−23839.
(26) Fan, L. F.; Zhang, C. Y.; Liang, G. F.; Yan, W. J.; Guo, Y. J.; Bi, Y. P.; Dong, C. *Sens. Actuators, B* **2021**, *334*, No. 129652.

(27) Zhang, Y. Y.; Chen, Y. E.; Hou, L. L.; Guo, F. Y.; Liu, J. C.; Qiu, S. S.; Xu, Y.; Wang, N.; Zhao, Y. *J. Mater. Chem. A* **2017**, *5*, 16134−16138.
(28) Zhou, A. W.; Dou, Y. B.; Zhao, C.; Zhou, J.; Wu, X. Q.; Li, R. J. *Appl. Catal., B* **2020**, *264*, No. 118519.
(29) Li, P. P.; Cao, Y.; Mao, C. J.; Jin, B. K.; Zhu, J. J. *Anal. Chem.* **2019**, *91*, 1563−1570.
(30) Shen, S. H.; Chen, J.; Wang, M.; Sheng, X.; Chen, X. Y.; Feng, X. J.; Mao, S. S. *Prog. Mater. Sci.* **2018**, *98*, 299−385.
(31) Chang, W. D.; Liu, W. P.; Shen, H. R.; Chen, S. S.; Liao, P. Z.; Liu, Y. J. *Anal. Chim. Acta* **2020**, *1112*, 46−53.
(32) Zhang, K.; Fan, Z. Q.; Yao, B.; Ding, Y. D.; Zhao, J.; Xie, M. H.; Pan, J. B. *Biosens. Bioelectron.* **2021**, *178*, No. 113019.
(33) Chen, J. S.; Ma, E. B.; Harrington, L. B.; Costa, M. D.; Tian, X. R.; Palefsky, J. M.; Doudna, J. A. *Science* **2018**, *360*, 436−439.
(34) Liang, M. D.; Li, Z. L.; Wang, W. S.; Liu, J. K.; Liu, L. S.; Zhu, G. L.; Karthik, L.; Wang, M.; Wang, K. F.; Wang, Z.; Yu, J.; Shuai, Y. T.; Yu, J. M.; Zhang, L.; Yang, Z. H.; Li, C.; Zhang, Q.; Shi, T.; Zhou, L. M.; Xie, F.; Dai, H. Q.; Liu, X. T.; Zhang, J. Y.; Liu, G.; Zhou, Y.; Zhang, B. C.; Liu, C. L.; Li, S. S.; Xia, X.; Tong, Y. J.; Liu, Y. W.; Alterovitz, G.; Tan, G. Y.; Zhang, L. X. *Nat. Commun.* **2019**, *10*, No. 3672.
(35) Li, S. Y.; Cheng, Q. X.; Wang, J. M.; Li, X. Y.; Zhang, Z. L.; Gao, S.; Cao, R. B.; Zhao, G. P.; Wang, J. *Cell Discovery* **2018**, *4*, 20.
(36) Xiong, Y.; Zhang, J. J.; Yang, Z. L.; Mou, Q. B.; Ma, Y.; Xiong, Y. H.; Lu, Y. *J. Am. Chem. Soc.* **2020**, *142*, 207−213.
(37) Peng, S.; Tan, Z.; Chen, S. Y.; Lei, C. Y.; Nie, Z. *Chem. Sci.* **2020**, *11*, 7362−7368.
(38) Shi, K.; Xie, S. Y.; Tian, R. Y.; Wang, S.; Lu, Q.; Gao, D. H.; Lei, C. Y.; Zhu, H. Z.; Nie, Z. *Sci. Adv.* **2021**, *7*, No. eabc7802.
(39) Li, K.; Huang, Z. Y.; Zeng, X. Q.; Huang, B. B.; Gao, S. M.; Lu, J. *ACS Appl. Mater. Interfaces* **2017**, *9*, 11577−11586.
(40) Vu, N. N.; Kaliaguine, S.; Do, T. O. *ACS Appl. Energy Mater.* **2020**, *3*, 6422−6433.
(41) Tang, Q.; Meng, X. F.; Wang, Z. Y.; Zhou, J. W.; Tang, H. *Appl. Surf. Sci.* **2018**, *430*, 253−262.
(42) Szczepankiewicz, S. H.; Moss, J. A.; Hofmann, M. R. *J. Phys. Chem. B.* **2002**, *106*, 2922−2927.
(43) Li, Y. B.; Zhang, H. M.; Liu, P.; Wang, D.; Li, Y.; Zhao, H. J. *Small* **2013**, *9*, 3336−3344.
(44) Li, K.; Gao, S. M.; Wang, Q. Y.; Xu, H.; Wang, Z. Y.; Huang, B. B.; Dai, Y.; Lu, J. *ACS Appl. Mater. Interfaces* **2015**, *7*, 9023−9030.
(45) Dong, Y. X.; Cao, J. T.; Wang, B.; Ma, S. H.; Liu, Y. M. *ACS Appl. Mater. Interfaces* **2018**, *10*, 3723−3731.
(46) Wang, M.; Ju, P.; Li, J. J.; Zhao, Y.; Han, X. X.; Hao, Z. M. *ACS Sustainable Chem. Eng.* **2017**, *5*, 7878−7886.

https://doi.org/10.1021/acs.analchem.1c02395
Anal. Chem. 2021, 93, 11816−11825